JOURNAL OF AIRCRAFT
Vol. 29, No. 6, Nov.–Dec. 1992

Multigrid Euler Calculations over Complete Aircraft

D. M. Tidd* and D. J. Strash*
Analytical Methods, Inc., Redmond, Washington 98052
and
B. Epstein,† A. Luntz,‡ A. Nachshon,§ and T. Rubin§
Israel Aircraft Industries Ltd., Ben Gurion Airport, 70100 Israel

A three-dimensional Euler code is applied to a series of configurations of increasing complexity. Comparisons are made to experiments, or to other computations when the former is not available. The method uses the multigrid approach on sets of equally spaced Cartesian grid cells. A unique and robust implementation of the body surface boundary condition on grid cells not aligned with the surface provides accurate results on relatively coarse grids. All computational results are compared to experimental data with good agreement exhibited over a wide range of flight conditions. The solution accuracy is assessed for the Onera M-6 wing, with errors due to grid resolution of less than 1% being achieved for the lift and pitching moment coefficients.

Nomenclature

$\boldsymbol{D}$ = $(\rho, \rho u, \rho v, \rho w, \rho e)$—vector of Euler variables
$\boldsymbol{E}$ = Euler spatial vector operator
e = energy
p = pressure
$\boldsymbol{q}$ = (u, v, w)—velocity vector in global coordinates
γ = 1.4
ρ = density

Introduction

THIS paper describes the application of a multigrid Euler solver to three configurations of increasing complexity, including two complete aircraft. Results have been obtained for a variety of flight conditions in the transonic flow regime, and comparisons with available data are presented. The code uses a unique surface boundary condition implementation on a simple grid structure that does not require the alignment of grid cells to the body surface.

The code has been constructed with the objective of creating a practical engineering tool capable of analyzing arbitrary configurations and providing rapid feedback to the engineer involved in aircraft design. The use of Cartesian grid cells, which may be sheared or rotated, effectively eliminates the labor-intensive task of grid generation, thus dramatically reducing the turnaround time to less than a week for a complete aircraft configuration.

Most current methods use structured or unstructured grids that must be fitted in some manner to the body surface. The present technique uses the multigrid approach to interrelate a set of local grids, ensuring consistent numerical solutions on all multigrid levels. The finest grids are generally positioned in high-curvature regions and the flow areas of interest. A given configuration is treated as a Boolean sum of components that may intersect, thus allowing the geometry to be prepared in a modular fashion. The intersections are treated automatically by the code and need not be previously defined by the user. The surface geometry is defined using a paneling strategy that is sufficiently dense to define the surface. In contract to most body-fitted grid techniques, there is no explicit relation between the surface paneling and the local grid cell structure. This means that many geometry modifications can be carried out without having to redefine the computational grids.

The next two sections of this article provide a brief outline of the numerical formulation and code structure. A more detailed discussion was presented previously in Refs. 1 and 2. Results are presented for configurations that exhibit increasing complexity, ranging from the ONERA M-6 wing to the F-18 fighter aircraft. The performance of the code is assessed by comparisons with experiment and published computational results.

Methodology

The equations solved are the three-dimensional Euler equations combined with the state equation, which can be written as

$$\boldsymbol{D}_t + \boldsymbol{E} = 0 \tag{1}$$

$$e = p/\rho(\gamma - 1) + \boldsymbol{q}^2/2 \tag{2}$$

Symmetrical schemes are used in the spatial discretization to provide a second-order accurate approximation of the derivatives. The dissipative terms are introduced for numerical stability following the technique described in Ref. 3, with the modification that only second-order finite differences are utilized.[4]

The discretized equations are solved by the modified four-stage Runge-Kutta scheme, with residual smoothing used to increase the CFL number.[1,3] The solution iteration process proceeds through the various grids using multigrid "V" cycles. If a solution is sought at level N, a Runge-Kutta iteration is performed at level N followed by a fine-to-coarse interpolation in which the field values are transferred from level N to a coarser level N-1. A Runge-Kutta iteration is then carried out on the coarser level N-1, proceeding to the coarsest grid at level 1.

To complete the "V" cycle, a similar transfer of variables from a level N-1 to a level N is used by means of a coarse-to-fine correction. Again, after each correction, a Runge-Kutta iteration is performed. Each Runge-Kutta iteration includes four stages of the time-marching scheme. After each

Received Aug. 15, 1991; presented as Paper 91-3236 at the AIAA 9th Applied Aerodynamics Conference, Baltimore, MD, Sept. 23–26, 1991; revision received Dec. 6, 1991; accepted for publication Dec. 6, 1991.

*Senior Research Scientist, 2133 152nd Avenue NE. Member AIAA.
†Head of CFD Group, Tashan Engineering Center, Aircraft Division. Member AIAA.
‡Senior Research Scientist, CFD Group, Tashan Engineering Center, Aircraft Division.
§Research Scientist, CFD Group, Tashan Engineering Center, Aircraft Division.

stage, a grid-overlap calculation is performed on the solution and a factorized residual smoothing is carried out on the correction. The dissipative terms are updated only once during the four Runge-Kutta stages.

The use of local refinement in the multigrid process, which includes Cartesian grid cells that may not be aligned with the body surface or with grid cells of other levels, gives rise to new problems associated with the exchange of information between grids. The most interesting of these is the treatment of overlapping grids contained in the same multigrid level. No restrictions on such overlaps are imposed; therefore, each flowfield point may belong to several overlapping grids. To ensure the proper exchange of information between grids at a common point, a "host grid" is chosen within which the point is most deeply embedded. The complete set of grids at each multigrid level is involved in the construction of the surface boundary condition implementation.

This approach ensures that the calculation for the set of grids at the same multigrid level tends to behave as if it were one composite grid. This becomes exactly true if the grid points coincide in the regions of overlap, and in the absence of residual smoothing.

Far-field boundary conditions, which are applied at the faces of the coarsest grid of the multigrid set, are constructed using Riemann invariants in a manner similar to that in Ref. 4. At the other grid boundaries, Dirichlet conditions are used, and one Runge-Kutta iteration is performed for each grid to avoid the instability originating in the boundary reflections. Finally, the change in outer boundary conditions due to a coarser grid correction provides the necessary damping of the reflection and facilitates convergence of the complete process.

The unique implementation of the solid-surface boundary condition sets this technique apart from other Cartesian grid approaches and ensures the success of the method as a whole. The "multivalue dummy point" concept has been adopted to implement the slip boundary condition for grid cells nonaligned with the configuration surface. That is, for each grid point G located in the flowfield, the point D is called dummy if it is both hidden from the point G by the surface and belongs to the finite difference template of G. Figure 1 illustrates one of the dummy points of a particular grid point G.

A local coordinate system is constructed at the point of intersection of segment GD with the configuration surface, by the normal n to the surface and two orthogonal vectors in the tangent plane. In these coordinates, the components of the velocity vector are ϕ, ψ, and χ respectively. A point D^* is constructed corresponding to a reflection of the point D through the tangent plane containing t. The components of velocity at the point D^* results from a linear extrapolation based upon the calculated values of ϕ, ψ, and χ at the selected points {Ri}. The value at the dummy point can then be determined directly from the information that χ is zero at the surface point GD. The pressure is extrapolated to D based on the normal momentum equation. In the above discussion, the surface point P is approximated by S, the intersection of the tangent plane with n. This approximation leads to poor resolution of the flow in areas of high curvature when coarse

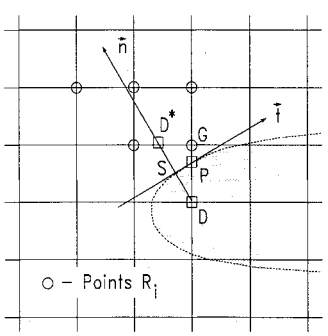

Fig. 1 Body surface boundary condition implementation.

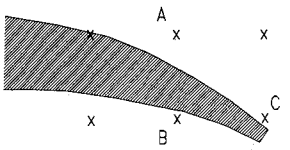

Fig. 2 Example of a multivalued dummy point.

grids are used. On finer grids, the distance between the points P and S is smaller, and therefore, smooth flow conditions are achieved.

Because the dummy point D described above is actually a grid point, the code allows for the common situation that a dummy point may be multivalued. An example of a dummy point B having three values is illustrated in Fig. 2. In this case, B is simultaneously a real point (since it is in the flowfield), a dummy point for grid point A, and a dummy point for grid point C.

A description of the mathematics used to assemble the dummy point formulae from the collection of points {Ri} is described below.

Let $F_t = (x_t, y_t, z_t)$ be the target point for which a formula is to be built, and let $F_i = (x_i, y_i, z_i)$, $i = 1, \ldots N$ be the selected grid points that participate in the formula. The required value at the target point u_t is obtained from the given values at the grid points u_i by the equation

$$u_t = \sum_{i=1}^{N} \alpha_i u_i \tag{3}$$

where α_i, $i = 1, \ldots N$ are a set of coefficients.

Equation (3) is exact for a constant field if the coefficients satisfy

$$\sum_{i=1}^{N} \alpha_i = 1 \tag{4}$$

Similarly, Eq. (3) is exact for a linear field if the coefficients satisfy both Eq. (4) and

$$\sum_{i=1}^{N} \alpha_i F_i = F_t \tag{5}$$

Under normal circumstances, the number of grid points N is greater than four, and therefore, there are more than one set of coefficients that satisfy the conditions in Eqs. (4) and (5).

To improve stability, the set of coefficients α_i with the minimum norm is chosen. This norm is defined as a weighted sum of the squares of the coefficients α_i with weights determined by the distances squared between the grid points and the target point, i.e.

$$\sum_{i=1}^{N} \alpha_i^2 |F_i - F_t|^2 \tag{6}$$

where

$$|F_i - F_t|^2 = (x_i - x_t)^2 + (y_i - y_t)^2 + (z_i - z_t)^2 \tag{7}$$

Code Structure

For increased user efficiency, the code[5] consists of two distinct stages. First, a preprocessor, that deals with each grid separately, determines which points are inside the configuration and which are outside (i.e., real points). For each real point, appropriate dummy and intersection points are found. The preprocessor also determines the grid relationships, the interpolation functions between grids, and the final boundary condition formula. The input procedure of the preprocessor

is easily implemented and includes extensive checks on the geometry and multigrid structure before the calculation proceeds. The preprocessor creates a data file that may be accessed by a graphics postprocessor to view the resulting aircraft configuration and grid geometry.

In the second stage, the multigrid Euler solver uses the preprocessor information to obtain the flowfield solution at a prescribed flight condition. Additional grids may be easily combined with the existing multigrid set at both the preprocessor and solver stages. Thus, additional mesh density or multigrid levels may be added without repeating previously calculated results.

Results

In this section, results from three different configurations exhibiting increasing complexity are presented. Calculations are compared with experiment and with other computations, depending upon availability.

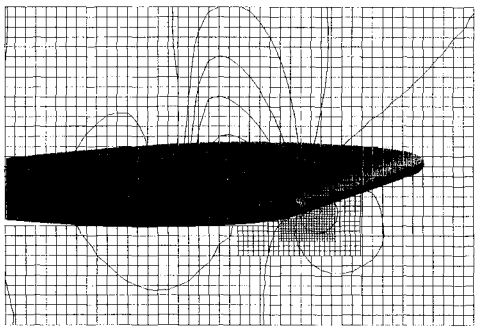

Fig. 3 Leading-edge resolution at levels 5, 6, and 7 for Onera M-6 wing.

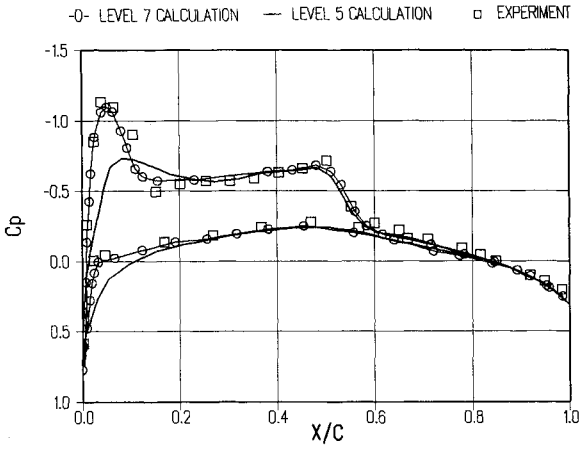

Fig. 4 Onera M-6 wing pressures at $y = 0.53$.

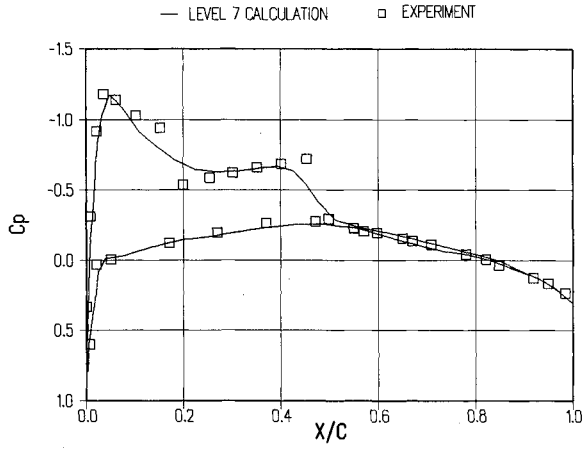

Fig. 5 Onera M-6 wing pressures at $y = 0.78$.

ONERA M-6 Wing

The ONERA M-6 wing,[6] which has been used to validate other Euler and Navier-Stokes codes (e.g., Ref. 7), provides a basis for examining the shock-capturing capabilities of the technique. Figure 3 presents a view of the M-6 wing, together with portions of multigrid levels 5–7, and illustrates the leading-edge resolution. The flight conditions for comparison with experiment are a Mach number of 0.84 and an angle of attack of 3.06 deg.

Figure 4 compares the computed and experimental pressure distributions at a wing location of 0.44 semispan ($y = 0.53$ m). The ONERA wing has both a swept shock parallel to the leading edge and a normal shock extending across the span. These two shocks converge in the outer span region close to the tip. The calculation accurately predicts the double shock structure present at this flight condition.

Accurate resolution of the leading-edge suction peak required the level 7 multigrid density (see Fig. 3), but the general flow features beyond 20% chord were well-defined at multigrid level 5 (see Fig. 4). The results at the multigrid level 5 stage illustrate the effect of the boundary condition approximation described in the Methodology section of this article because the leading edge is clearly the region of highest curvature, with flow variables varying rapidly.

Experimental and calculated pressure distributions at spanwise location $y = 0.78$ are compared in Fig. 5. The calculated

Table 1 Onera M-6—effect of grid density on lift coefficient

Solution	CL	Percentage error		
		a	*b*	*c*
Level 3	0.2206	18.54	18.87	19.19
Level 4	0.2433	10.16	10.52	10.89
Level 5	0.2538	6.28	6.65	7.03
Level 6	0.2668	1.48	1.86	2.27
Level 7	0.2692	0.59	0.98	1.39
Infinite grid[a]	0.2708	0.00	—	—
Infinite grid[b]	0.2719	—	0.00	—
Infinite grid[c]	0.2730	—	—	0.00

[a]This calculation. [b]Reference 7. [c]Reference 7.

Table 2 Onera M-6—effect of grid density on pitching moment coefficient

Solution	CM	Percentage error
Level 3	−0.1721	14.68
Level 4	−0.1849	8.33
Level 5	−0.1905	5.55
Level 6	−0.1994	1.14
Level 7	−0.2008	0.45
Infinite grid	−0.2017	0.00

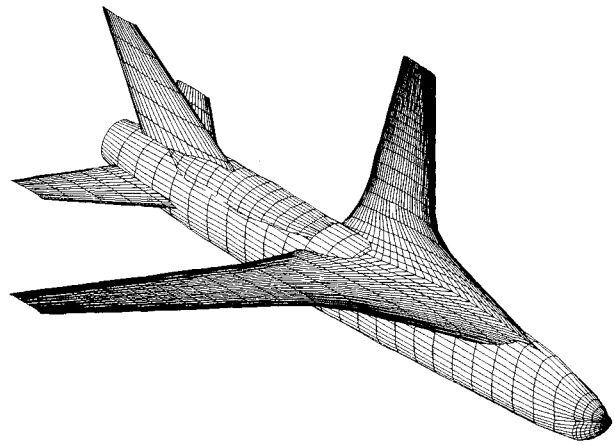

Fig. 6 Supercritical-wing research airplane.

shock location at this station is correctly predicted; however, the shocks have been smeared over 10–15% chord. Both the current level 6 and level 7 grids do not extend far enough aft of the leading edge to resolve the shock. There may also be some viscous effects, because in the outermost spanwise locations of the wing, there appears to be a small bubble of overpredicted C_p at the base of the shock, which is characteristic of inviscid solutions.

In order to examine the accuracy and convergence of the compared results, the values of the coefficients of lift are shown in Table 1. The values on the three finest grid levels are accurate to three decimal places. Included in Table 1 are estimates of the errors at various grid refinement levels, using computed infinite grid values, because no experimental data are available. The errors were first calculated against the infinite grid values described in Ref. 7, where results from two Navier-Stokes codes are presented. The infinite grid predictions were obtained from a second-order Richardson extrapolation in which the extrapolation was based on the cube root of the total number of cells in the field. Since the computations described here are based on local refinement in a Cartesian framework, it was decided that it was more appropriate to base the extrapolation on the cube root of the cell sizes (i.e., $\sqrt[3]{DX \times DY \times DZ}$, where DX, DY, and DZ are the cell sizes in the three directions). The percentage errors of the computed lift coefficients against all three of the infinite grid solutions are shown in Table 1. The computed error on the finest level 7 grid yields an error of less than 1.5% in all cases.

Table 2 shows a comparison of the computed pitching moment coefficient at the various grid levels, together with the error analysis using an infinite grid value. The moments were taken about the inboard leading edge.

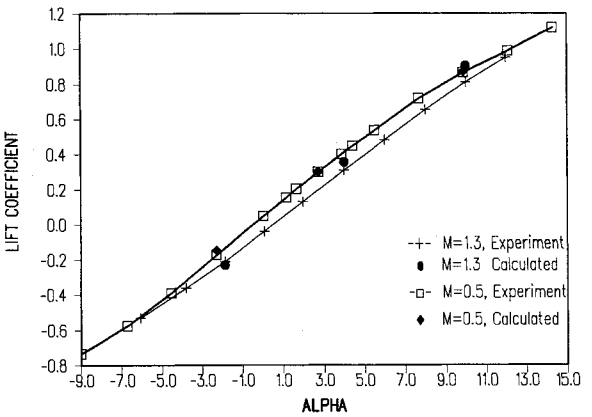

Fig. 7 Research airplane lift curve slopes at Mach 0.5 and 1.3.

NASA Supercritical-Wing Research Airplane

An extensive series of wind-tunnel investigations were carried out on the TF-8A research airplane with a supercritical wing at a range of flight conditions. A series of reports on these investigations have appeared (e.g., Refs. 8 and 9). The airplane geometry as described for the calculations is illustrated in Fig. 6.

For the present calculations, two representative Mach numbers were chosen in order to validate the code on a complete aircraft configuration. The resulting lift curve slopes for Mach numbers of 0.5 and 1.3, together with the experimental comparisons, are illustrated in Fig. 7. There is particularly good agreement at the subsonic Mach number, with the higher Mach number also yielding acceptable results to engineering accuracy. The presented results are from calculations up to multigrid level 7. As with the previous example, the finest grids at levels 6 and 7 are placed only over the areas of highest curvature. The grids at level 5 are illustrated in Fig. 8, where three overlapping grids were used.

The computed chordwise pressure coefficient distribution at Mach 0.5 and an angle-of-attack of 2.73 deg over an inboard section of the wing is compared with the experiment in Fig. 9. The calculations show excellent agreement at this location, which corresponds to 30.7% span. Further outboard there is

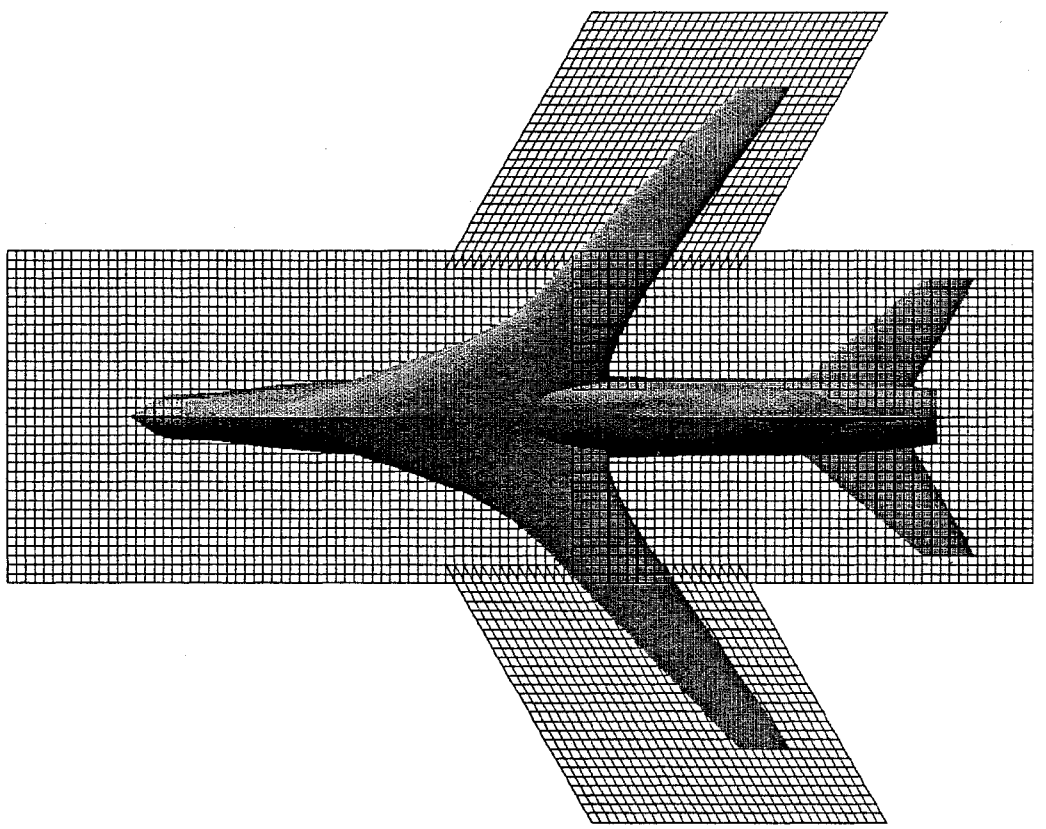

Fig. 8 Level 5 grid resolution for research airplane.

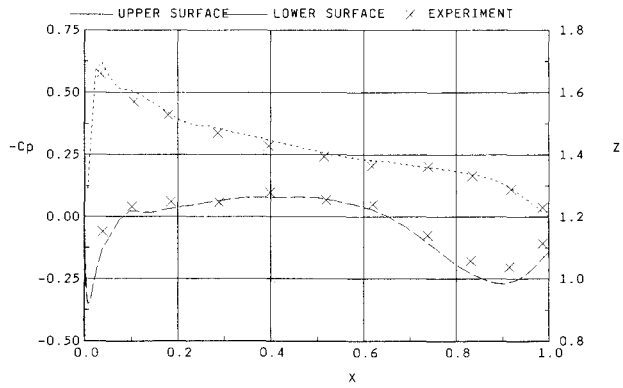

Fig. 9 Research airplane pressures at 30.4% span.

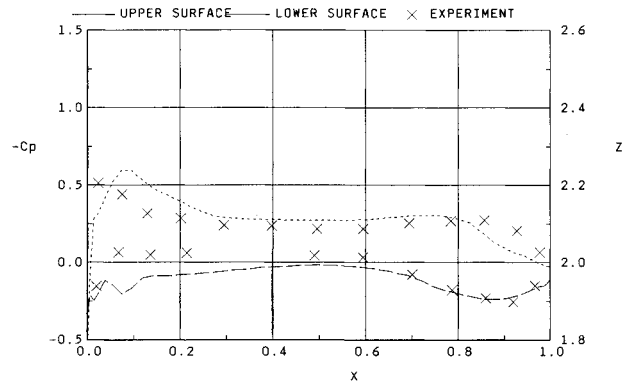

Fig. 10 Research airplane pressures at 80.4% span.

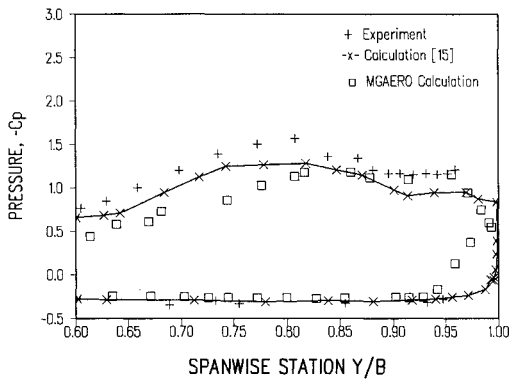

Fig. 11 F-18 pressures on LEX at $x = 235.5$.

less agreement (see Fig. 10), which corresponds to a wing section at 80.4% span.

The finest grid in the set used at level 7 was a swept grid along the leading edge with the same cell size in the X (longitudinal) direction and Z (vertical) direction. From Fig. 8, it can be seen that the chord length and maximum thickness vary significantly from inboard to outboard. Hence, based on number of grid points across the chord, the grid density is twice as coarse at 80% span compared to 30% span. For accurate pressure distributions in this area, a further grid refinement is required.

F-18 Fighter

The F-18 is a complex fighter configuration and has been the subject of other calculations (e.g., Refs. 10 and 11). Initial calculations on this aircraft at low angles of attack provided no problems for the technique. Validation of the numerical discretization was accomplished by carrying out calculations of the lift curve slope in the linear range at subsonic Mach numbers. Comparisons were made with available data and with other calculations from a subsonic panel method code.[12] The calculations showed agreement similar to the previous examples described in this paper.

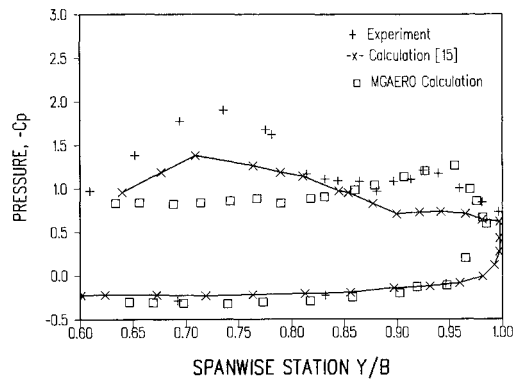

Fig. 12 F-18 pressures at LEX at $x = 296.5$.

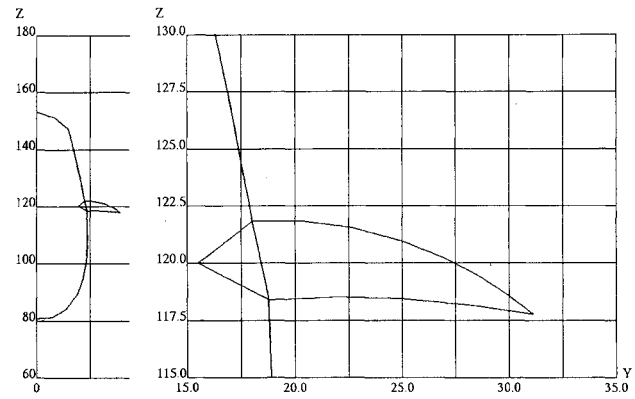

Fig. 13 LEX geometry and level 6 grid density at $x = 235.5$.

The main area of interest for this aircraft is controllable flight at high angles of attack. Much work has been carried out to investigate the contribution toward this aim of the wing leading-edge extension (LEX).[11] Current results have been obtained at a Mach number of 0.2 and an angle of attack of 19 deg. Surface pressures from this run are presented at two axial stations on the LEX in Figs. 11 and 12.

In these figures, comparisons are made to experiment and to the Navier-Stokes computations presented in Ref. 11. The computations described in Ref. 11 were for a geometry that contained only the forebody and LEX. The present calculations show the correct qualitative features, especially in the tip area, where the LEX vortex initiates.

Further inboard, the calculations are in less agreement, which indicates that the reverse flow of the vortex is not fully resolved. The LEX geometry at the cut location $x = 235.5$, corresponding to Fig. 11, is shown in Fig. 13, where the use of intersecting components in the code can also be seen, with the LEX modeled as a separate component to the fuselage. Also illustrated in Fig. 13 is the grid resolution around this cut location, with the grid lines indicating the multigrid level 6 density.

The inviscid code has predicted the separation from the sharp leading edge of the LEX with the artificial viscosity providing a means of resolving the vortical flow. The agreement is reasonable, given the grid density and the low Mach number of the run. Further refinement may resolve the flow better, although it is known that, for too fine a grid, the artificial viscosity will not have the required effects.

Resource Requirements

The computer requirements for the cases described in this article are summarized in Table 3. The CPU time is quoted as a ratio relative to the longest solver run in the printed results, which represents an overnight run on modern-day workstations. The solver times are approximately the time required to converge to a solution yielding four significant

Table 3 Computer requirements

Level	M-6 5	M-6 7	TF-8A 7	F-18 6
Grid points (thou-	289	344	366	378
sands)	52	60	68	76
Core memory (Mbytes)	0.16	0.04	0.26	0.17
CPU prep	0.38	0.43	1.00	0.83
CPU solver				

figures of accuracy in the force and moment coefficients. Solver calculations are carried out at different flight conditions without repeating the preprocessor run.

The CPU times for the M-6 are provided for two different grid level calculations with the times for the finer level 7 grid performed using the code's restart option. The additional level 6 and level 7 grids were placed over only the wing leading edge, with no refinement in the spanwise direction (refinement in the other two directions is shown in Fig. 3). As further grid levels are added, the multigrid "V" cycles become larger, and hence the solver CPU time required per level increases.

The code works entirely in core by taking advantage of virtual memory capabilities, and the elapsed time for the calculations can increase by as much as a factor of two, depending upon the amount of core memory available. The total number of grid points includes grid points that are inside the configuration; therefore, this cannot, in general, be directly used to determine the number of unknowns.

Conclusions

The results described in this article illustrate that use of Cartesian grid cells may be regarded as a practical technique when used in a multigrid approach. The code has been shown to be capable of accurately computing the flow about complex configurations for engineering applications, and for the analysis of complete aircraft. The code has demonstrated an accurate shock-capturing capability in the transonic regime by using local grid refinement. Through an evolutionary process, the basic shock location emerges at coarse grid levels and the shock structure may be refined by the addition of finer grids. Such procedures are easily implemented within the multigrid structure because additional mesh density or multigrid levels may be added while taking into account previously computed results.

The grid resolution study on the M-6 wing indicates that if sufficient local refinement is carried out on the wing leading edge, accurate predictions of the suction peak can be accomplished within the Cartesian mesh framework. The solution accuracy was estimated by using infinite grid predictions, and errors of less than 1% were found in the lift and pitching moment coefficients on the finest computational mesh.

Acknowledgments

The authors thank David Lednicer of AMI for his assistance in preparing the Research Airplane and F-18 geometries.

References

[1]Epstein, B. Luntz, A., and Nachshon, A., "Multigrid Euler Solver about Arbitrary Aircraft Configurations, with Cartesian Grids and Local Refinements," AIAA Paper 89-1960, Buffalo, NY, June 1989.

[2]Epstein, B., Luntz, A., and Nachshon, A., "Euler Solver for Arbitrary Configurations: Further Applications," *Proceedings of Israeli Conference on Aeronautics and Astronautics*, Tel Aviv, Haifa, Israel, 1990.

[3]Jameson, A., Schmidt, W., and Turkel, E., "Numerical Solution of the Euler Equations by Finite Volume Methods Using Runge-Kutta Time-Stepping Schemes," AIAA 14th Fluid and Plasma Dynamics Conf., AIAA Paper 81-1259, Palo Alto, CA, 1981.

[4]Jameson, A., and Baker, T. J., "Solution of the Euler Equation for Complex Configurations," AIAA Paper 83-1929, 1983.

[5]Strash, D. J., and Tidd, D. M., *MGAERO Users' Manual*, Version A2, Analytical Methods, Inc., Redmond WA, June 1991, Chap. 3.

[6]Schmitt, V., and Charpin, F., "Experimental Data Base for Computer Program Assessment," AGARD-AR-183, May 1979, Chap. B1.

[7]Bonhaus, D. L., and Wornom, S. F., "Relative Efficiency and Accuracy of Two Navier-Stokes Codes for Simulating Attached Transonic Flow over Wings," *AIAA 8th Applied Aerodynamics Conference*, AIAA Paper 90-3078-CP, Portland, OR, 1990.

[8]Barlett, D. W., and Re, R. J., "Wind-Tunnel Investigation of Basic Aerodynamic Characteristics of a Supercritical-Wing Research Airplane Configuration," NASA TM X-2470, Feb. 1972.

[9]Harris, C. D., "Wind-Tunnel Measurements of Aerodynamic Load Distribution on a NASA Supercritical-Wing Research Airplane Configuration," NASA TM X-2469, Feb. 1972.

[10]Cenko, A., Tseng, W., Phillips, K., and Madson, M., "Tranair Applications to Transonic Flowfield Predictions," 29th Aerospace Sciences Meeting, AIAA Paper 91-0201, Reno NV, Jan. 7–10, 1991.

[11]Cummings, R., Schiff, L., Rizk, Y., and Chaderjian, N., "Numerical Simulation of High-Incidence Flow Over the F-18 Aircraft," ICAS-90-3.3.1, Stockholm, Sweden, Sept. 1990.

[12]Maskew, B., *Program VSAERO Theory Document*, NASA CR-4023, 1985.